Journal of Molecular Catalysis A: Chemical 423 (2016) 143–150

Contents lists available at ScienceDirect

Journal of Molecular Catalysis A: Chemical

journal homepage: www.elsevier.com/locate/molcata

Water splitting behavior of copper-cerium oxide nanorods and nanocubes using hydrazine as a scavenging agent

S.L. Clavijo-Chaparro[a,b], A. Hernández-Gordillo[c], R. Camposeco-Solis[a], V. Rodríguez-González[a,*]

[a] División de Materiales Avanzados, Instituto Potosino de Investigación Científica y Tecnológica, Camino a la Presa San José 2055, Col. Lomas 4a. sección, C.P. 78216 San Luis Potosí, S.L.P., Mexico
[b] Grupo de Investigaciones en Minerales, Biohidrometalurgia y Ambiente – GIMBA, Universidad Industrial de Santander- UIS, Sede Guatiguará, Transversal Guatiguará, Calle 8N N° 3W-60, Barrio El Refugio, C.P. 681011, Piedecuesta, Santander, Colombia
[c] Instituto de Investigaciones en Materiales, Universidad Nacional Autónoma de México, Av. Universidad 3000, Copilco, 04510 Cd. de México D.F., Mexico

ARTICLE INFO

Article history:
Received 24 March 2016
Received in revised form 21 May 2016
Accepted 13 June 2016
Available online 17 June 2016

Keywords:
Photocatalytic water splitting
Cerium oxide nanostructures
Hydrothermal assisted microwave method
Hydrogen

ABSTRACT

A one-step microwave synthesis using neither a template surfactant nor strong molar NaOH concentrations is reported. Well shaped nanorod and nanocube CeO_2 structures were achieved in 0.5 and 4 h at a maximum irradiation of 200 W, respectively. Both nanostructures grew through different processes, they are dependent on the irradiation conditions, time and temperature. The photocatalytic water splitting evaluation of cerium oxide nanostructures was carried out using water contaminated with hydrazine and the surface *"in-situ"* functionalization of Cu^0 nanoparticles (CuNPs) on the surface, achieving 753 μmol/h g of hydrogen generation. During the photocatalytic process, the "*in-situ*" reduction reaction ($CuO \rightarrow Cu^0$) occurring on the CeO_2 surface promotes the electron transfer process due to the copper work function.

1. Introduction

In the last decade, the microwave synthesis of materials has been increasingly used because of the fast synthesis of hierarchical nanostructures with 0 to 3D morphologies and high crystallinity [1,2]. The use of acid or basic synthesis media and surfactants as structure directors has been reported [3]. Mixed oxide nanostructures such as TiO_2, SiO_2, $CaTiO_3$, etc. have been successfully synthesized by the hydrothermal assisted microwave method (Hy-MWM) and used in applications such as water depollution, air purification, sensors and photocatalytic water splitting among many other applications [4–8].

Nowadays, CeO_2 modified with Ni or NiPt or CoPt metal nanoparticles results in an effective catalyst for the decomposition of hydrous hydrazine into hydrogen at room temperature. Pure CeO_2 shows no catalytic activity for the decomposition of N_2H_4 systems, but the deposited metal nanoparticles modify its electronic properties and, as a consequence, increase its catalytic characteristics [9–11], although cerium oxide structures have been scarcely synthesized by the Hy-MWM [12–17]. Typically, the synthesis of ceria is performed at temperatures of 80–160 °C under strong alkaline conditions with high power irradiations (300–900 W), varying the pressure (1.2–14 atm). In some cases, polyethylene glycol (PEG) [14] or an ethylene glycol (EG) [15] template is used to obtain ceria with either well-nanocrystallized or amorphous phases with nanosphere, nanorod, and nanocube morphologies. However, these ceria nanostructures have not been functionalized with copper nanoparticles and never tested in photocatalytic water splitting.

The present communication features the use of the Hy-MWM to synthesize cerium oxide at low power and at two different temperatures, using a surfactant-free or organic template, and low molar NaOH. Nanorod-like or nanocube structures were obtained depending on the synthesis temperature and reaction time. Cu_xO_y UV-photoassisted deposition and the "*in-situ*" reduction to Cu^0 over both cerium oxide nanostructures was carried out in order to evaluate the photoactivity in the water splitting hydrogen production from water contaminated with hydrazine and irradiated with UV-light. The efficiency of the Cu^0-CeO_2 nanorod-like structures in the H_2 production is discussed as a function of the surface properties.

* Corresponding author.
E-mail address: vicente.rdz@ipicyt.edu.mx (V. Rodríguez-González).

http://dx.doi.org/10.1016/j.molcata.2016.06.011
1381-1169/

2. Materials and methods

2.1. Hydrothermal synthesis of CeO_2 nanostructures

Cerium oxide morphologies were synthesized by the Hy-MWM. Briefly, 0.539 M cerium nitrate (10 mL) and 6.90 M NaOH (70 mL) aqueous solutions were prepared using distilled water and stirred separately for 20 min. Then, the alkaline solution was poured into a 150-mL-Teflon vessel, and then the cerium aqueous solution was added dropwise. The resulting mixture was stirred magnetically for 30 min and then placed in ultrasonic bath for 5 min. The vessel containing the final suspension was placed into a microwave reactor (Eyela MWO-1000 Wave Magic) and heated by microwave irradiation at 125 °C for nanorod-like and 180 °C for nanocube structures and a maximum variable microwave irradiation power of 200 W with 700 rpm was chosen. The optimized microwave irradiation times for homogeneous nanorod (NR) or nanocube (NC) morphologies were 0.5 and 4.0 h, respectively. The precipitated powders were cooled at room temperature, recovered by centrifugation at 400 rpm and vacuum filtered using a microporous membrane (Pall, GH polypropylene, 0.2 μm) and washed several times with deionized water and ethanol in order to remove the sodium ions. Finally, the solid was dried at 80 °C overnight.

2.2. Functionalization of Cu_xO_y NPs on CeO_2 surface catalysts

Photodeposition of Cu_xO_y nanoparticles was carried out as follows; an ethanol solution of $CuNO_3$, keeping a load of 1 wt.% Cu, and 50 mg of either NRs or NCs, previously prepared by the Hy-MWM, were placed in a small glass reactor. The suspension was placed under vigorous stirring for 5 min and then in ultrasonic bath for 5 min to ensure the complete disaggregation of agglomerated particles. Afterwards, the slurry was maintained under magnetic stirring at 500 rpm for 1 h and, at the same time, irradiated with a 17 W UVC lamp (TecnoLite G15T8, 254 nm, 1168 μW/cm^2). Then, the suspension was filtered using a hydrophilic polypropylene filter (Pall, 0.2 μm) in a vacuum system. The solids were completely dried overnight in an oven at 80 °C and identified as Cu/NR and Cu/NC.

2.3. Characterization of CeO_2 and Cu_xO_y/CeO_2 nanostructures

XRD patterns were recorded using a Bruker discover X-ray diffractometer with Cu Kα irradiation of 1.5406 Å, operated at 35 kV and 25 mA over the 20–90° range. The morphology and nanostructure analyses of the as-obtained CeO_2 were performed by means of FESEM and HRTEM, respectively. FESEM images were obtained on a Helios Nanolab microscope equipped with a field emission gun and EDX analyzer operated at 5 kV. The HRTEM images were obtained with a FEI Tecnai F30 microscope equipped with a tungsten field emission gun operated at 300 keV. Band gap energy values were obtained from UV–vis-DRS spectra using a UV–vis-NIR Agilent Technologies Cary 5000 spectrophotometer equipped with integration sphere. The Kubelka–Munk method was employed for the band gap energy calculations. The XPS analysis was performed by using a K-Alpha Thermo Scientific system with Al Kα source (1486.68 eV) operating at 12 KV and 6 mA. All the binding energies were referenced to the C 1 s peak. Temperature programmed reduction was performed in a ChemBET TPR/TPD chemisorption analyser by Quantachrome Instruments within a temperature interval ranging from room temperature to 600 °C with a heating rate of 10 °C/min and flow of 30 mL/min of H_2 (10%)/Ar gas.

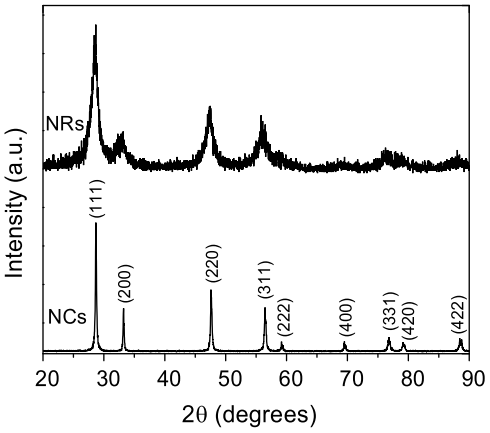

Fig. 1. XRD patterns of CeO_2 nanocrystals with different shapes.

2.4. Water splitting performance testing

The photocatalytic activities of the Cu^0/CeO_2 NRs and NCs were evaluated in a cylindrical home-made reactor with an inner quartz tube equipped with a UV Hg lamp (λ = 254 nm, I_0 = 4400 μwatts/cm^2). CeO_2 annealed from the initial mixture without irradiation was also tested in the photocatalytic reaction as an experimental blank. The glass reactor had a full operation volume of 200 mL and the solutions consisted of water-hydrazine hydrate 99.93 vol.% of H_2O dosed with 0.1 M of hydrazine (Fluka, 24–26 vol.%). In all the experiment runs, 0.03 g of powder (cerium NRs or NCs and Cu-NRs or Cu-NCs) were used and the suspension was purged with nitrogen for 20 min to remove the dissolved oxygen from the solution while it was stirred. Once oxygen was displaced, the reactor system was sealed and the UV lamp was turned on. To obtain the Cu^0NPs, the photodeposited Cu_xO_y NPs on CeO_2 wer reduced "*in-situ*" during the photocatalytic reaction. Hydrogen determination was done every hour for 8 h in a gas chromatograph by Thermo Scientific equipped with a TCD and column by Thermo Scientific Trace PLOT TG-BOND Msieve 5A. The system was previously calibrated in order to quantify the hydrogen production.

Three cycles of stability experiments of 8 h per cycle were carried out for the selected active Cu/NR. After running the experiments, the UV lamp was turned off, the produced hydrogen was released and the reaction system was purged with nitrogen until the hydrogen chromatography signal disappeared. Then, the reactor system was sealed and the lamp was turned on again to start the next cycle and so on until the three cycles were completed.

3. Results and discussion

3.1. Structural features

In Fig. 1, the XRD patterns for the NRs and NCs are shown. Both patterns exhibit the cubic fluorite-type structure of CeO_2 obtained by hydrothermal processes (ICDD 00-043-1002). Broad XRD peaks are observed for the NRs whose different crystallinity, in comparison with the NCs, may be attributed to the 1D morphology and the size of nanorods. No peaks from other crystalline phases or impurities are observed, which confirms the advantage of the Hy-MWM for the synthesis of inorganic materials [12]. The FESEM characterization shows the 1D morphology for the NRs (Fig. 2a) and a prismatic box that is perfectly faceted of various sizes, a 3D nanocube morphology (Fig. 2b). The NRs have an average diameter of 9.31 nm and a length of 75.9 nm. In the case of the NCs, the average edge size is 21.3 nm, (Fig. S1, ESI*). All the NR and NC structures seem well defined and solid, without being broken or incomplete

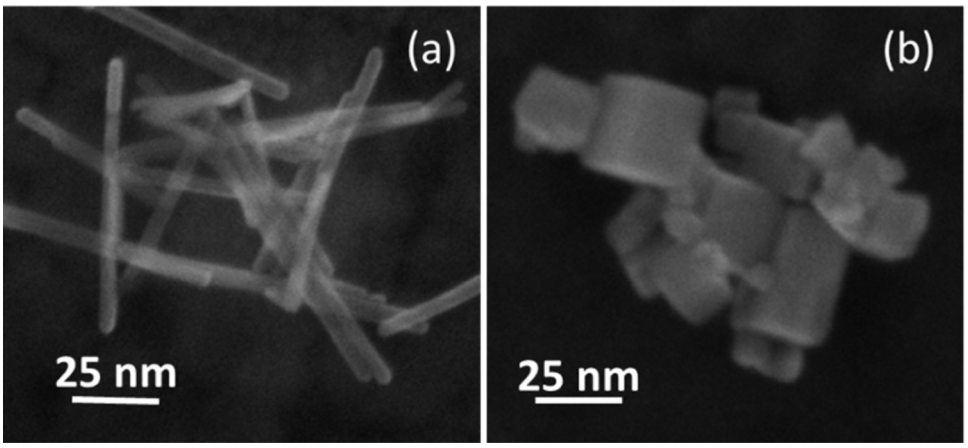

Fig. 2. SEM CeO_2 micrographs: a) NRs and b) NCs.

[18]. In order to confirm that both nanostructures did not have textural and/or morphological defects, an HRTEM examination was carried out.

The obtained images featured in Fig. 3(a) show the round ends of the NRs with their atomic indexed arrangement; in the case of the NCs, the plane fringes are also analogous, Fig. 3(b). As the two nanostructures grew through different processes, it can be said that they are dependent on the irradiation conditions, time and temperature. The Ostwald ripening followed the oriented attachment growth process for the formation of nanorods and a dissolution-recrystallization for nanocubes, (Fig. 4). The optimal parameters for obtaining NRs were 125 °C in 0.5 h. At low reaction time, we observed that amorphous nanoparticles were formed. However, when the reaction time was increased, the agglomeration of nanoparticles was carried out. The agglomeration and growth of CeO_2 nanoparticles with shorter reaction time has been also noted in previous investigations [12,15]. The growth mechanism was attributed to Ostwald ripening model. After 0.5 h of reaction, the nanostructures growth in preferential directions to become in NR, by an oriented attachment mechanism [12,15]. On the other hand, the reaction time and the operation temperature were increased to obtain nanocubes morphologies. As these conditions have been increased, nanocubes, nanorods and nanoparticles were simultaneously observed, which indicates that nanorods were dissolved in

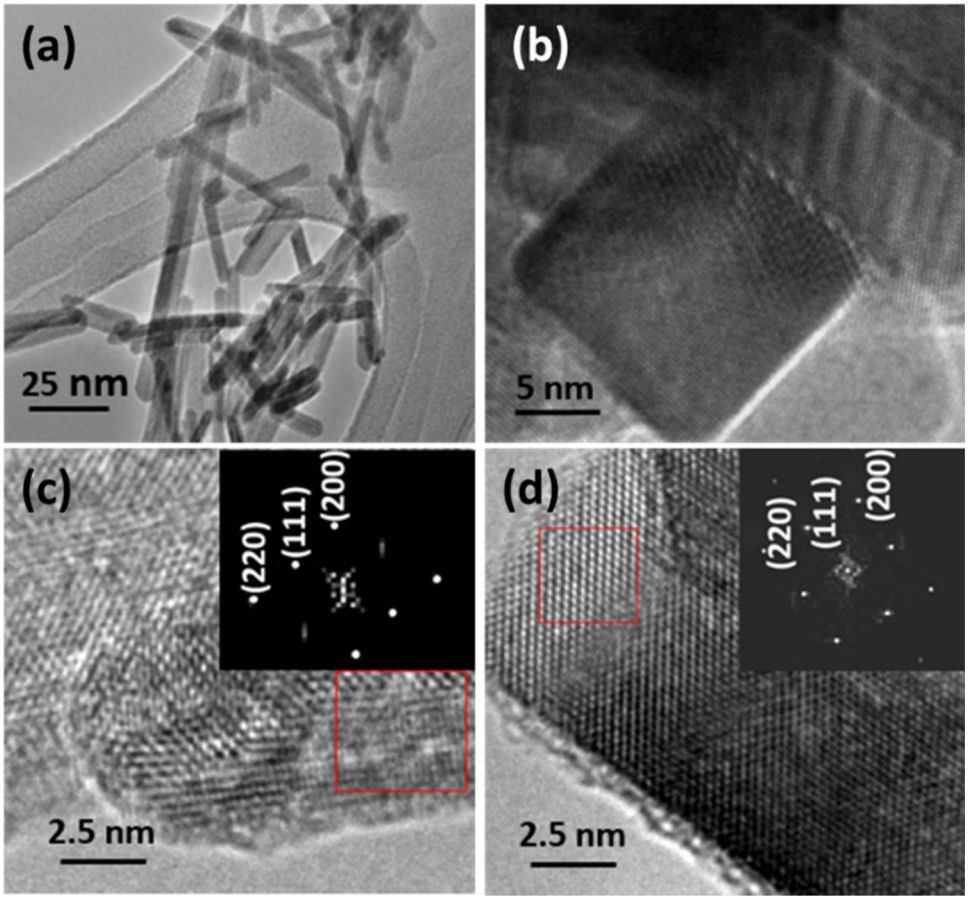

Fig. 3. HRTEM images of: a) and c) left side of NRs and b) and d) right side of NCs.

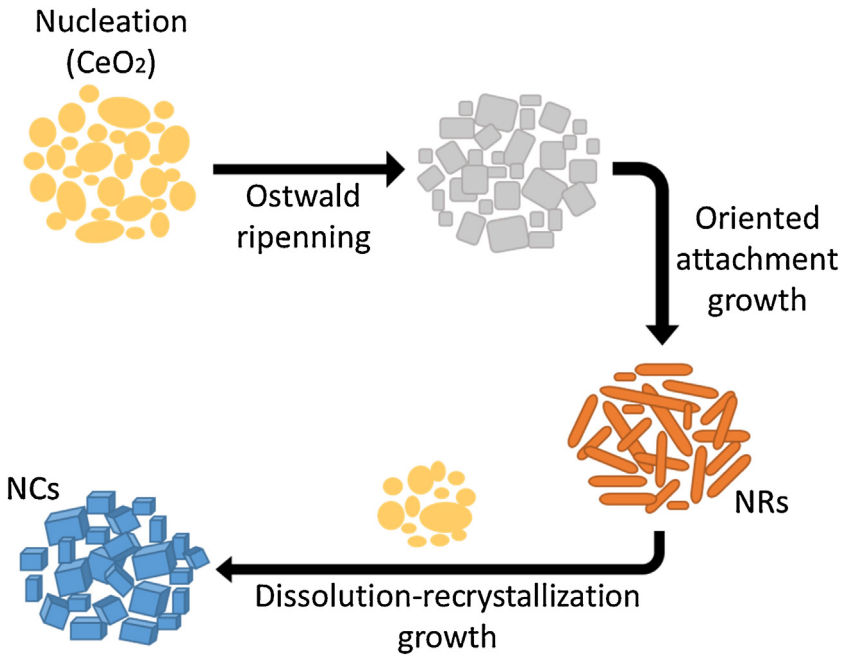

Fig. 4. Schematic illustration of the growth mechanism for CeO_2 nanocrystals, 30 min at 125 °C for nanorod-liked and 4 h at 180 °C for nanocube structures.

the medium and a process of recrystallization to the nanocubes formation occurred [19,20]. Only nanocubes were observed after 4 h of irradiation at a fixed temperature of 180 °C. A more energetic hydrothermal process favours the nanocube side growth, forming NCs and the recrystallization process needs more time. Longer times produce high crystalline structures as indicated by the XRD results.

The thermochemical effect of the temperature and time on the alkaline medium governs the nucleation growth and growth rate. A more alkaline medium, 10 M, did not enhance the growth rate; in fact, the NCs or NRs were observed as bigger and incomplete specimens. In addition, a time increase enhanced neither the structure nor the morphology, and either dissolution or recrystallization may occur, promoting the formation of damaged nanostructures [21]. A more energetic hydrothermal process favours the nanocube side growth, forming NCs and the recrystallization process needs more time, 4 h. Longer times produce high crystalline structures as indicated by the XRD results. Well-shaped nanocubes were obtained in 4 h at 180 °C.

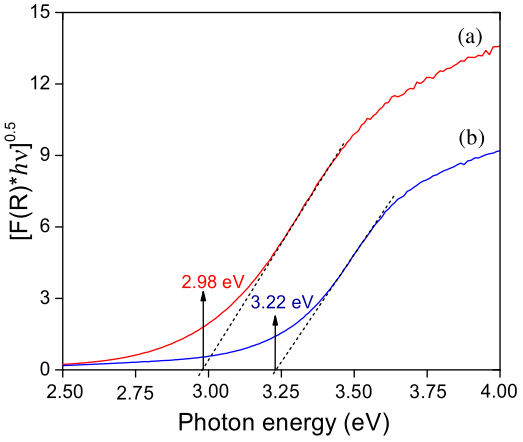

Fig. 5. Tauc plot of a) NRs and b) NCs.

The Tauc Plot is featured in Fig. 5, which shows that the NR absorption occurred at 360–450 nm, whereas for the NCs, the absorption was blue shifted, which corresponds to band-gap energies of 2.98 and 3.22 eV, respectively. The ceria absorption in the UV region was originated from a charge transfer transition between O_{2p} and Ce_{4f} states in Ce^{4+} [15]. However, the absorption edge of the NRs at 400 nm suggests the presence of Ce^{3+} species in the sample, which originates low band gap activation energies that arise from $Ce^{3+} \longleftarrow O^{2-}$, although Ce^{3+} like Ce_2O_3 has been discarded by XRD analyses [22]. This fact indicates that the absorption edge positions depend on the Ce^{4+} and Ce^{3+} contents in CeO_{2-x}. In the case of copper oxides/CeO_2, the absorption behavior and band gap energies are the same, which suggests that CeO_2 did not manifest any change and the presence of Cu_xO_y was not observed either.

3.2. Catalytic activity

The specific surface area is high for the NRs (115 m^2/g) and very low for the NCs (17.6 m^2/g). The NR and NC photoactivities were evaluated in the photocatalytic production of hydrogen (H_2) using a hydrazine/water system and the surface photodeposition of Cu_xO_y nanoparticles (CuNPs) dispersed on the surface (Fig. 6). The CeO_2 nanorods, CeO_2 nanocubes and CeO_2 obtained by calcination did not show photocatalytic activity, which was similar to photolysis, Fig. 6(a). The Cu_xO_y deposition promoted the photoactivity of CeO_2 NR nanostructures, yielding H_2 production. Considering that the sample changed its light green colour to a dark grey colour, as the reaction time progressed, it was assumed that Cu_xO_y was reduced from Cu^+ to Cu^0 by the hydrazine reducing effect [23]. The CeO_2 nanorods modified with 1.0 wt.% Cu (Cu/NRs) showed the highest photocatalytic activity (753 μmol/h g), Fig. 6(b). This photoactivity could have been generated from the interaction between reduced Cu^0 and CeO_2 and from the NR highest specific surface area that allowed a high CuNP dispersion after the "*in-situ*" reduction of Cu_xO_y highly dispersed. The stability experiments showed that the Cu/NR photocatalyst was deactivated after 16 h of reaction (Fig. 6c).

Ce 3d XPS spectra from the NRs, NCs, Cu/NR and spent Cu/NRs are shown in Fig. 7a–d. Cu 2p and O 1 s XPS spectra from the NRs and NCs are shown in Fig. 8a–c. The interpretation of the Ce 3d spectra

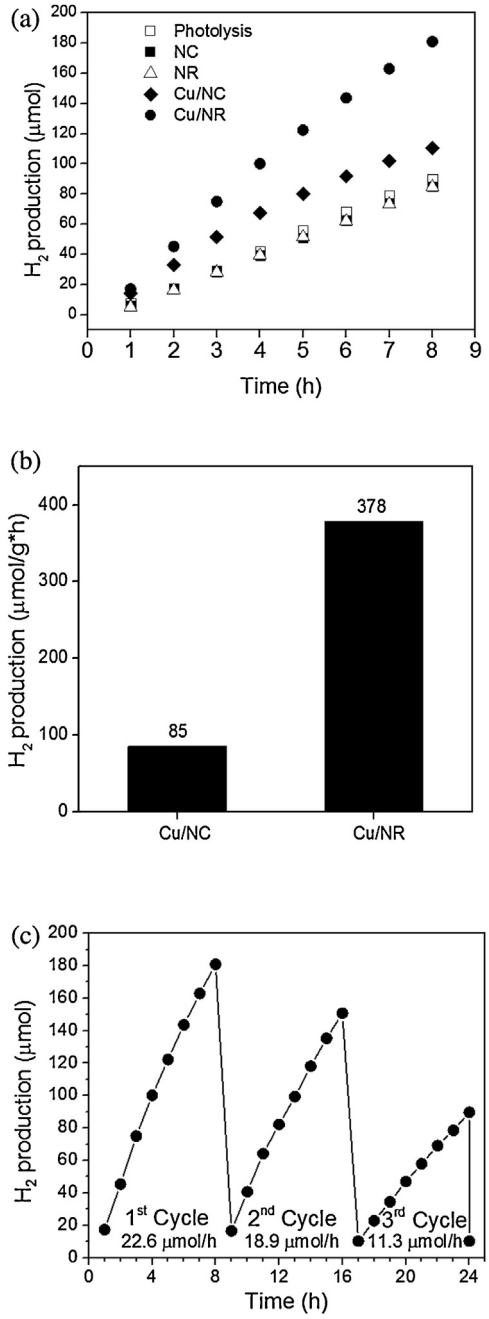

Fig. 6. H_2 production (µmol) for 8 h of reaction with: a) CeO_2 nanocrystals, b) H_2 production (µmol/g h) with Cu/NR and Cu/NC, and c) photocatalytic stability of Cu/NR for 24 h of reaction.

collected for cerium oxide accounts for the presence of ten peaks (Fig. 7). The v, vii, viii, u, uii and uiii peaks are attributed to Ce^{4+} species, while the ui peak is associated with the Ce^{3+} species [24]. The contribution of the Ce^{3+} and Ce^{4+} species can be determined from the ten peaks by solving the following equation: $Ce^{3+} = Ce^{3+}/Ce^{3+} + Ce^{4+}$ [25].

The deconvoluted XPS spectra of the Ce 3d are shown in Fig. 8(a–d). In the spectra of Ce 3d, there are six peaks for Cu/NR, NR, NC and spent Cu/NR photocatalysts, the peaks of Ce $3d_{3/2}$ are labeled by "u", while the others labeled by "v" originate from $3d_{5/2}$. The pairing (u', v') are characteristic of Ce^{3+}, likewise the other peaks are the different states of Ce^{4+}. From Figs. 8(a–d), it can be observed that the intensities of the signals of Ce^{3+} and Ce^{4+} are higher in all samples, indicating that Ce^{3+} and Ce^{4+} are the main

Table 1
The ratio Ce^{3+}/Ce^{4+} from Ce 3d spectra deconvolution of nanocrystals.

Sample	Ce^{+3}/Ce^{+4} ratio
Cu/NR	1.9
NR	1.6
NC	1.5
Spent Cu/NR	1.3

oxidation state. In Table 1 the ratio Ce^{3+}/Ce^{4+} was listed for the Cu/NR, spent Cu/NR, NR and NC samples. These facts indicate a Ce^{3+} enrichment on the NR surface [26,27].

In addition, the O 1 s spectra for the NC samples exhibit the main peak at 529.5 eV, but as for the NR samples, an additional contribution at a high binding energy of 532.4 eV appears, hereafter labeled as O_{lat} (Fig. 8a). These changes indicate a progressive oxidation of the NR samples, where the intensity of the O_{lat} peak decreases with reoxidation.

In Fig. 8b and c, the XPS spectrum of Cu 2p from the Cu/NR sample shows the main peak at around 933 eV (Cu $2p_{3/2}$). The Cu $2p_{3/2}$ peaks are composed of two individual peaks at 933 and 930 eV, where each one is related to different copper species. The peak at low binding energies (930 eV) indicates the presence of copper in the lowest valence state, which is related to Cu^0 in low proportion [28]. According to the deconvoluted Cu 2p spectra of Cu/NR, it is observed that the major proportion of Cu^+ species is Cu_2O follow of Cu^{2+} specie (CuO_2) in the Cu/NR sample due to the interface attachment of CuNPs on CeO_2 surface.

It is known that the oxidized Cu atoms are reduced by N_2H_4 because it provides a strongly reductive atmosphere to maintain the effectiveness of the catalyst [19,25]. However, the XPS spectrum for the spent catalyst exhibited a low proportion of both peaks at 933 and 930 eV, which are associated with Cu^+ and Cu^0, respectively, which indicate that part of the copper species was probably lixiviated during the reaction, causing the decrease in Cu contents, and as consequence, the photoactivity was decreased, Fig. 7c.

H_2-TPR of the samples were carried out in order to verify and support information of the presence of Cu species, Fig. 9. The H_2-TPR profiles display two peaks at 400 and 550 °C that can be observed in both CeO_2 samples. These peaks are ascribed to the reduction of surface and bulk Ce^{4+} species to Ce^{3+}, and Ce^{3+} species to Ce^0, respectively. However, Ce^{3+} is the predominant species in the NR sample, which is in agreement with XPS result [29,30].

The Cu/NC sample shows an intense reduction peak at around 260 °C, which can be associated to the reduction of isolated Cu^{+2} ions and the reduction of Cu^{+2} to Cu^{+1}; however, the reduction of either Ce^{4+} or Ce^{3+} was not observed.

By contrast, the Cu/NR sample shows a small reduction peak at around 260 °C, associated to the reduction of isolated Cu^{+2} ions and Cu^{+2} to Cu^{+1}, while we already, the high temperature intense peaks (>380 °C) corresponding to the reduction of Cu^{+1} to Cu°. This indicates that the Cu^{1+} is the predominant species on CuNR surface. However, after the photocatalytic reaction, in the spent sample photocatalyst, the characteristic peaks of the reduction of Cu^{+1} to Cu° decreased, suggesting that the quantity of Cu^{+1} species is low. This indicates that part of Cu^{+1} species was "*in-situ*" reduced to Cu^0 during the photocatalytic reaction as observed experimentally and could explain the low Cu^{+1} content observed in the XPS result, Fig. 8c [31].

3.3. Mechanism of H_2 production

According to the energy diagram, the position of the conduction band of CeO_2 (−0.5 V) is more negative than the redox potential of the H^+/H_2 couple (0.0 V) at pH = 0 [32], and therefore, the electron transfer process can be carried out when CeO_2 is photoactivated by

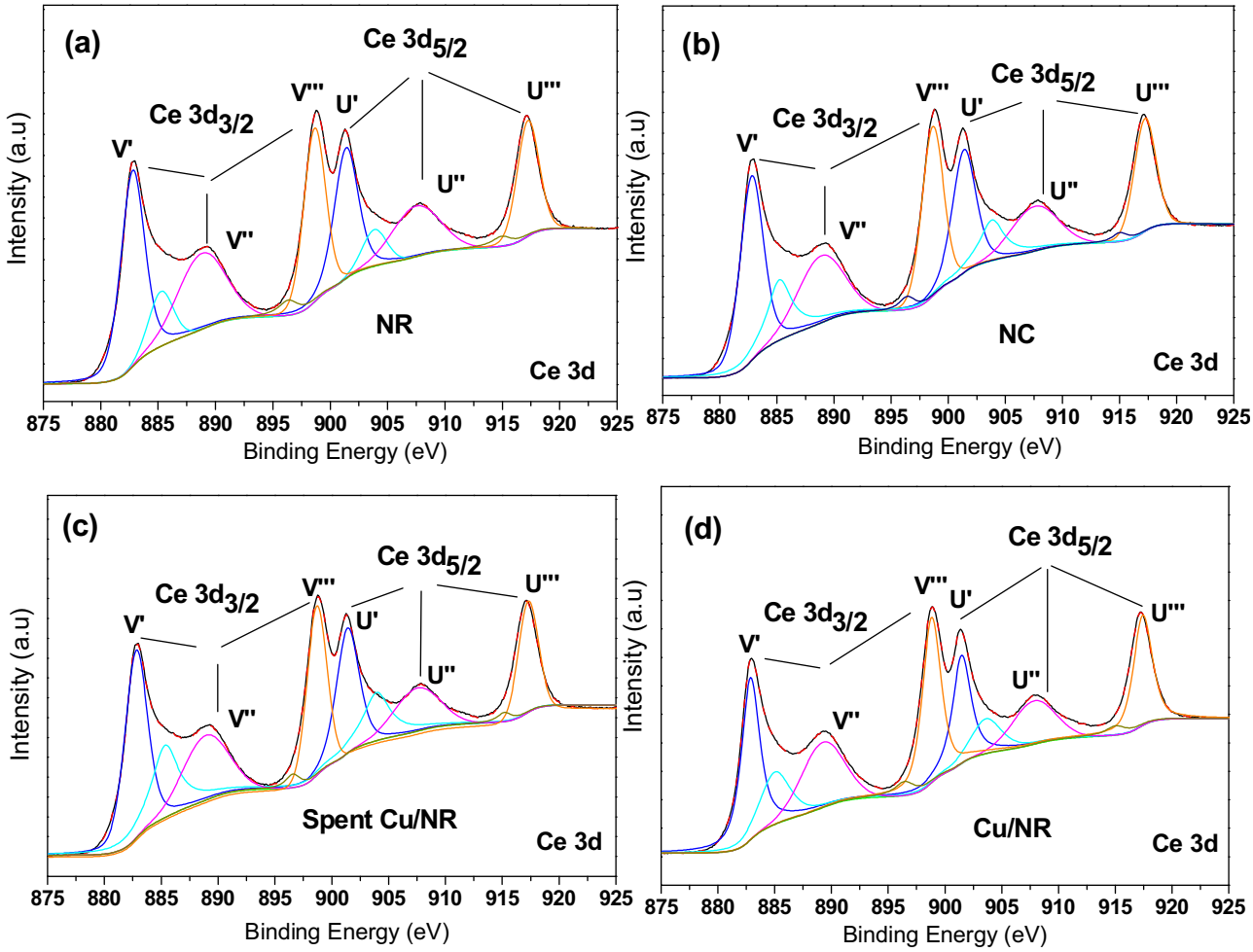

Fig. 7. a) Ce 3d, b) O 1s, c) Cu 2p and d) Cu 2p deconvoluted XPS spectra of CeO_2 nanocrystals.

UV–vis light irradiation. However, the electron transfer is limited and as consequence, the electron-hole combination occurs and the H_2 production is not observed as occurred with the reference TiO_2-P25 [33]. Conversely, when the CeO_2 NR and NC semiconductors are functionalized with CuNPs by reduction "in-situ", the photocatalytic H_2 production, in the presence of hydrazine, follows a similar previously reported mechanism [20]. During the irradiation process, the reduction reaction ($CuO \rightarrow Cu^0$) occurring on the CeO_2 surface promotes the electron transfer process due to the copper work function that is shown in the graphical abstract (4.5–4.7 eV) [30].

In this case, when the Cu^0NPs are in contact with the CeO_2 semiconductor, the photogenerated electrons and holes flow and build up a new equilibrium state, in which the Fermi level, work function of Cu^0 (4.5–4.7 eV), and redox potential of H_2/H_+ are in equilibrium [34]. Then the space-charge region builds up in the semiconductor photocatalyst and helps separate the electrons and holes.

Because of the band-gap excitation state, the h^+ photogenerated on the semiconductor reacts with hydrazine to form the hydrazyl radical (NH_2NH^*) until yielding tetrazane [35], while the photogenerated electrons (e^-) flow to the metal nanoparticles to be transferred to the acceptor protons (H^+), yielding an efficient separation of the charge carriers, and achieving the H_2 generation, see the graphical abstract.

4. Conclusions

In summary, the present research features a practical way to control the nanostructure morphology derived from the hydrothermal reaction assisted by microwave irradiation in a short time. By controlling the microwave irradiation time in alkaline medium (6.9 M NaOH), the following structures were obtained: i) well-faceted CeO_2 nanocubes with 23.1-nm sides (17.6 m^2/g), on average, at 180 °C in 4 h, or ii) CeO_2 nanorods with an average diameter of 9.3 nm and length of 75.9 nm (115 m^2/g) in only 0.5 h at 125 °C. The photocatalytic behavior of CeO_2 nanorods functionalized with 1.0% of low-cost CuO (Cu/NR) showed a photoactivity rate of 753 μmol/h g of hydrogen generation. XPS and H_2-TPR measurements confirm the ratio Ce^{3+}/Ce^{4+} that enhanced the H_2 photoproduction on Cu/NR nanocrystals.

It is expected that further experiments on *in-situ* doping of copper into cerium titanate or activated with visible irradiation will allow hydrogen generation for more than 24 h.

Acknowledgements

We gratefully acknowledge G. Labrada-Delgado, B. Rivera-Escoto and H. Silva Pereyra from LINAN-IPICYT for the FESEM, XRD and HRTEM characterizations. The authors thank M. Hinojosa-Reyes for helping with the hydrogen experiments. S. L. Clavijo-Chaparro thanks CONACYT for the undergraduate student

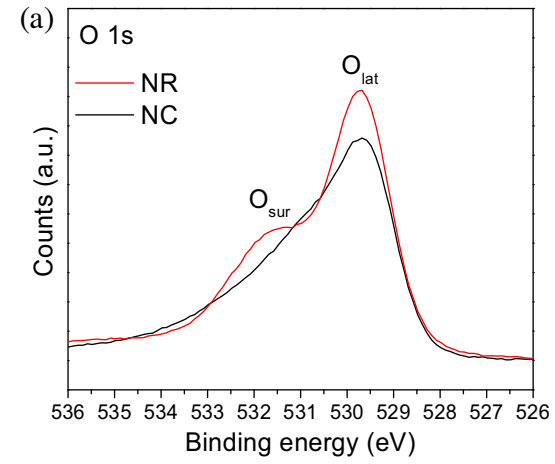

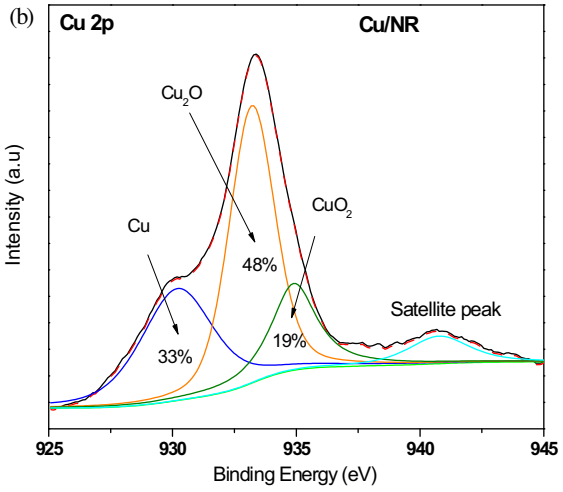

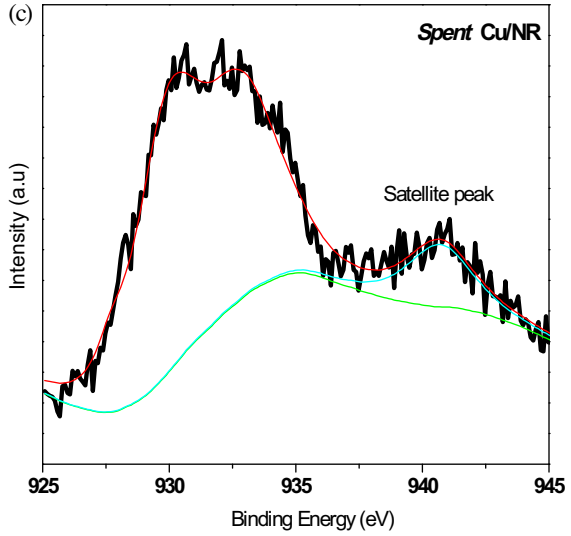

Fig. 8. Ce 3d deconvoluted XPS spectra of Cu/NR and nanocrystals.

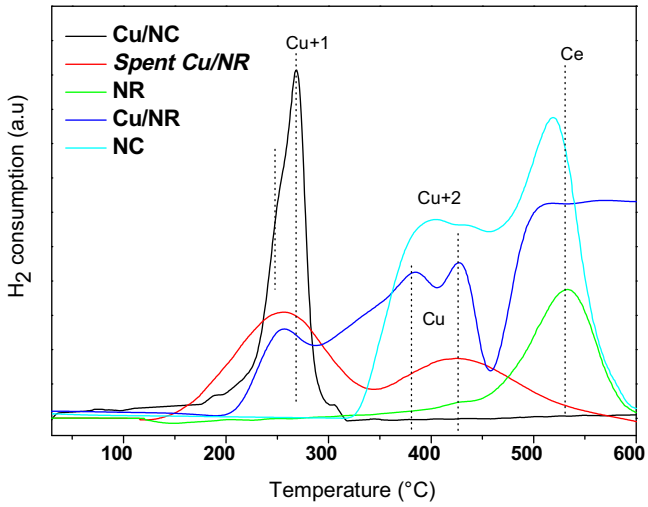

Fig. 9. H_2-TPR profiles of CuNPs/CeO_2 and CeO_2 nanocrystals.

scholarship 20758 from the CB-2011/169597SEP and CONACYT-2014 S-2780 projects.

Appendix A. Supplementary data

Supplementary data associated with this article can be found, in the online version, at http://dx.doi.org/10.1016/j.molcata.2016.06.011.

References

[1] T.-D. Nguyen, C.-T. Dinh, D. Mrabet, M.-N. Tran-Thi, T.-O. Do, Controlled synthesis of ceria nanoparticles for the design of nanohybrids, J. Colloid Interface Sci. 394 (2013) 100–107.
[2] M. Selvakumar, D. Krishna, Microwave synthesized nanostructured TiO_2-activated carbon composite electrodes for supercapacitor, Appl. Surf. Sci. 263 (2012) 236–241.
[3] A.N. Kadam, R.S. Dhabbe, M.R. Kokate, Y.B. Gaikwad, K.M. Garadkar, Preparation of N doped TiO_2 via microwave-assisted method and its photocatalytic activity for degradation of malathion, Spectrochim. Acta A 133 (2014) 669–676.
[4] R.M. Mohamed, E.S. Aazam, Photocatalytic oxidation of carbon monoxide over NiO/SnO2 nanocomposites under UV irradiation, Int. J. Photoenergy 2012 (2012) 1–9.
[5] L.M. Lozano-Sánchez, S.-W. Lee, T. Sekino, V. Rodríguez-González, Practical microwave-induced hydrothermal synthesis of rectangular prism-like $CaTiO_3$, CrysEngComm 15 (2013) 2359–2362.
[6] R.C. Deus, M. Cilense, C.R. Foschini, M.A. Ramirez, E. Longo, A.Z. Simões, Influence of mineralizer agents on the growth of crystalline CeO_2 nanospheres by the microwave-hydrothermal method, J. Alloys Compd. 550 (2013) 245–251.
[7] W. Mahmoud, A. Faidah, Microwave assisted hydrothermal synthesis of engineered cerium oxide nanopowders, J. Eur. Ceram. Soc. 32 (2012) 3537–3541.
[8] R.C. Riccardi, P.R. dos Santos, J.A. Bueno, E. Longo, Preparation of CeO2 by a simple microwave–hydrothermal method, Solid State Ionics 180 (2009) 288–291.
[9] H.-L. Wang, J.-M. Yan, Z.-L. Wang, S.-I. O, Q. Jiang, Highly efficient hydrogen generation from hydrous hydrazine over amorphous $Ni_{0.9}Pt_{0.1}/Ce_2O_3$ nanocatalyst at room temperature, J. Mater. Chem. A 1 (2013) 14957–14962.
[10] L. He, B. Liang, L. Li, X. Yang, Y. Huang, A. Wang, X. Wang, T. Zhang, Cerium-oxide-modified nickel as a non-noble metal catalyst for selective decomposition of hydrous hydrazine to hydrogen, ACS Catal. 5 (2015) 1623–1628.
[11] O. Song-Il, J.-M. Yan, H.-L. Wang, Z.-L. Wang, Q. Jiang, High catalytic kinetic performance of amorphous CoPt NPs induced on CeO_x for H_2 generation from hydrous hydrazine, Int. J. Hydrogen Energy 39 (2014) 3755–3761.
[12] D. Araújo, W. Avansi, H.B. de Carvalho, M.L. Moreira, E. Longo, C. Ribeiro, M.I.B. Bernardi, CeO_2 nanoparticles synthesized by a microwave-assisted hydrothermal method: evolution from nanospheres to nanorods, CrystEngComm 14 (2012) 1150–1154.
[13] F. Bonamartini Corradi, A.M. Bondioli, Synthesis and characterization of nanosized ceria powders by microwave–hydrothermal method, Mater. Res Bull. 41 (2006) 38–44.

[14] M.L. Dos Santos, R.C. Lima, C.S. Riccardi, R.L. Tranquilin, P.R. Bueno, J.A. Varela, E. Longo, Preparation and characterization of ceria nanospheres by microwave-hydrothermal method, Mater. Lett. 62 (2008) 4509–4511.
[15] Y. Tao, H. Wang, Y. Xia, G. Zhang, H. Wu, G. Tao, Preparation of shape-controlled CeO_2 nanocrystals via microwave-assisted method, Mater. Chem. Phys. 124 (2010) 541–546.
[16] E. Kumar, P. Selvarajan, D. Muthuraj, Synthesis and characterization of CeO_2 nanocrystals by solvothermal route, Mater. Res. 16 (2013) 269–276.
[17] Y. Tao, F.H. Gong, H. Wang, H.P. Wu, G.L. Tao, Microwave-assisted preparation of cerium dioxide nanocubes, Mater. Chem. Phys. 112 (2008) 973–976.
[18] S.L. Clavijo-Chaparro, Síntesis de nanoestructuras de óxido de cerio por el método hidrotérmico asistido por microondas y su evaluación en la producción fotocatalítica de hidrógeno, in: Tesis Licenciatura, Universidad Industrial de Santander, 2014.
[19] T.M. Laura, A. Gilbanka, B. Puertolas, T. Garcia, Shape-dependency activity of nanostructured CeO_2 in the total oxidation of polycyclic aromatic hydrocarbons, Appl. Catal. B-Environ. 132–133 (2013) 116–122.
[20] H.-X. Mai, L.-D. Sun, Y.-W. Zhang, R.S. Wei Feng, H.-P. Zhang, H.-C. Liu, C.-H. Yan, Shape-selective synthesis and oxygen storage behavior of ceria nanopolyhedra, nanorods, and nanocubes, J. Phys. Chem. B 109 (2005) 24380–24385.
[21] M.-H. Oh, J.-S. Nho, S.-B. Cho, J.-S. Lee, R.K. Singh, Novel method to control the size of well-crystalline ceria particles by hydrothermal method, Mater. Chem. Phys. 124 (2010) 134–139.
[22] N.K. Renuka, A.K. Praveen, C.U. Aniz, Ceria rhombic microplates: synthesis, characterization and catalytic activity ceria rhombic microplates: synthesis, characterization and catalytic activity, Microp. Mesop. Mater. 169 (2013) 35–41.
[23] A. Hernández-Gordillo, V. Rodríguez-González, Silver nanoparticles loaded on Cu-doped TiO_2 for the effective reduction of nitro-aromatic contaminants, Chem. Eng. J. 261 (2014) 53–59.
[24] J. Xu, J. Harmer, G. Li, T. Chapman, P. Collier, S. Longworth, S.-C. Tsang, Size dependent oxygen buffering capacity of ceria nanocrystals, Chem. Commun. 46 (2010) 1887–1889.
[25] J.L. Gasser-Ramirez, B.C. Dunn, D.W. Ramirez, E.P. Fillerup, G.C. Turpin, Y. Shi, R.D. Ernst, R.J. Pugmire, E.M. Eyring, K.A. Pettigrew, D.R. Rolison, J.M. Harris, A simple synthesis of catalytically active: high surface area ceria aerogels, J. Non. Cryst. Solids. 354 (2008) 5509–5514.
[26] J.P. Holgado, G. Munuera, J.P. Espinós, A.R. González-Elipe, XPS study of oxidation processes of CeOx defective layers, Appl. Surf. Sci. 158 (2000) 164–171.
[27] S. Watanabe, X. Ma, C. Song, Characterization of structural and surface properties of nanocrystalline TiO2-CeO2 mixed oxides by XRD, XPS, TPR, and TPD, J. phys. chem. C 113 (2009) 14249–14257.
[28] A. Piras, S. Colussi, A. Trovarelli, V. Sergo, J. Llorca, R. Psaro, L. Sordelli, Structural and morphological investigation of ceria-promoted Al2O3 under severe reducing/oxidizing conditions, J. Phys. Chem. B 109 (2005) 11110–11118.
[29] R. Fu, N. Yoshizawa, M.S. Dresselhaus, G. Dresselhaus, J.H. Satcher, T.F. Baumann, XPS study of copper-doped carbon aerogels, Langmuir 18 (2002) 10100–10104.
[30] J.X. Qin, Z.M. Wang, X.Q. Liu, Y.X. Li, L.B. Sun, Low-temperature fabrication of Cu(I) sites in zeolites by using a vapor-induced reduction strategy, J. Mater. Chem. A 3 (2015) 12247–12251.
[31] T.Q. Kang, P. Wang, L. Li, K. Liu, M. Li Chang, Photocatalytic reduction of carbon dioxide by hydrous hydrazine over Au–Cu alloy nanoparticles supported on $SrTiO_3/TiO_2$ coaxial nanotube arrays, Angew. Chemie Int. Ed. 54 (2015) 841–845.
[32] Y. Xu, M.A.A. Schoonen, The absolute energy positions of conduction and valence bands of selected semiconducting minerals, Am. Mineral. 85 (2000) 543–556.
[33] S. Oros-Ruiz, R. Zanella, R. López, A. Hernández-Gordillo, R. Gómez, Photocatalytic hydrogen production by water/methanol decomposition using Au/TiO2 prepared by deposition-precipitation with urea, J. Hazard. Mater. 263 (2013) 2–10.
[34] Y. Zhang, Lim Chen, R.-S. Liu, D.P. Tsai, Plasmonic photocatalysis, Rep. Prog. Phys. 76 (046401) (2013) (41pp).
[35] Y. Oosawa, Photocatalytic hydrogen evolution from aqueous hydrazine solution over precious-metal/anatase catalysts, J. Chem. Soc. Faraday Trans. 1 (1984) 1507–1515.